IEEE Transactions on Quantum Engineering

Received 21 March 2024; revised 10 June 2024; accepted 15 August 2024; date of publication 20 August 2024; date of current version 9 September 2024.

Digital Object Identifier 10.1109/TQE.2024.3445967

Simulation of Charge Stability Diagrams for Automated Tuning Solutions (SimCATS)

FABIAN HADER[1], SARAH FLEITMANN[1], JAN VOGELBRUCH[1], LOTTE GECK[1,2], AND STEFAN VAN WAASEN[1,3]

[1]Central Institute of Engineering, Electronics and Analytics—Electronic Systems, Forschungszentrum Jülich GmbH, 52425 Jülich, Germany

[2]Faculty of Electrical Engineering and Information Technology, RWTH Aachen University, 52062 Aachen, Germany

[3]Faculty of Engineering—Communication Systems, University of Duisburg-Essen, 47057 Duisburg, Germany

Corresponding author: Fabian Hader (e-mail: f.hader@fz-juelich.de).

ABSTRACT Quantum dots (QDs) must be tuned precisely to provide a suitable basis for quantum computation. A scalable platform for quantum computing can only be achieved by fully automating the tuning process. One crucial step is to trap the appropriate number of electrons in the QDs, typically accomplished by analyzing charge stability diagrams (CSDs). Training and testing automation algorithms require large amounts of data, which can be either measured and manually labeled in an experiment or simulated. This article introduces a new approach to the realistic simulation of such measurements. Our flexible framework enables the simulation of ideal CSD data complemented with appropriate sensor responses and distortions. We suggest using this simulation to benchmark published algorithms. Also, we encourage the extension by custom models and parameter sets to drive the development of robust technology-independent algorithms.

INDEX TERMS Automated tuning, charge stability diagram (CSD), quantum computing, semiconductor quantum dots (QDs).

I. INTRODUCTION

Quantum dot (QD) tuning automation is a crucial step to enable a scalable platform for quantum computation. Two essential steps are the isolation of electrons in QDs, hereafter referred to as dot regime tuning, and the adjustment of an appropriate number of electrons, referred to as charge state tuning below. One can observe the charge and spin states in gate-defined QDs by the conductance change of a nearby electrostatically coupled sensor dot. The development of tuning algorithms based on machine learning (ML) and classical algorithms, the assessment of the quality of a solution, and the comparison of different approaches benefit from publicly available datasets. Especially for the latter two purposes, this is even a prerequisite to enable fair comparability. Simulations can generate the required number of datasets along with the corresponding ground truth data. Therefore, we propose a generic framework for the simulation of charge stability diagrams (CSDs) that combines the necessary functionalities to mimic experimental data. To simulate the ideal CSD,[1] we introduce a geometric model, which does not require knowledge of the physical device parameters. Instead, it allows the reconstruction of measurement data merely based on parameters describing the geometry observed in previously recorded data.

The rest of this article is organized as follows. In Section II, we comprehensively introduce the different aspects of quantum simulation. In Section III, we describe our simulation model consisting of our geometric model for the double quantum dot (DQD) occupation (see Section III-A), a model for the sensor response (see Section III-B), and distortions (see Section III-C). In Section IV, we depict the extraction of parameters from measured data. In Section V, we evaluate the quality of the simulated data. Finally, in Section VI, we summarize our work and draw a conclusion comprising suitable application fields and prospective improvements. Code is available at https://github.com/f-hader/SimCATS.

II. BACKGROUND

Simulating quantum mechanical processes is a manifold and complex task, especially for many-body systems and their corresponding Hamiltonian, due to the exponential scaling of the required resources with the number of particles in the

[1]In this context, ideal refers to simulated undisturbed (ground truth) data.

system and the large number of environmental degrees of freedom. Several theories and models that describe different quantum mechanical processes include the Schrödinger equation (SEQ) and master equations (MEQs) for closed and open quantum systems [1], [2], [3], [4], Feynman path integrals [5], the density functional theory (DFT) [6], [7], [8], mean-field theories [9], [10], [11], nonequilibrium Green functions (GFs) [12], [13], [14], and the random/scattering matrix theory [15], [16], [17], [18]. Besides the time dynamics of the quantum states (described by SEQ and MEQ), the ground state (the eigenvector of the Hamiltonian with the smallest eigenvalue) is of fundamental interest and corresponds to the state when the system is at zero temperature. Principally, classical computers or quantum devices can be used for the simulation task [19].

Quantum simulators use a quantum system to model a Hamiltonian. They can be digital, i.e., they use a quantum computer with qubits and sequentially applied gates, or analog, i.e., the especially designed system emulates the Hamiltonian. The first approach is more general but requires thousands of highly controllable qubits. The second incorporates no gates and is easier to control but less versatile, on the other hand. Georgescu et al. [20] described a comprehensive overview of the proposed systems and potential application fields. Moreover, QD systems [21], [22] play an exciting role in this field recently, e.g., in simulating the low-temperature Hubbard model (HM) [23], emulating Fermi–Hubbard models [24], [25], [26], [27], demonstrating Nagaoka ferromagnetism [28], or simulating the antiferromagnetic Heisenberg chain [29], [30].

When using classical computer systems to simulate higher particle systems, numerical approximation approaches must be used. Here, the challenge is to find the balance between exactness, computation cost, applicability to the problem, and validity of results. Methods proposed for this task comprise quantum Monte Carlo (MC) approaches [7], [8], [31], [32], many-body perturbation theories [33], [34], multiconfiguration time-dependent Hartree [35], [36], [37], hierarchical equations of motion [38], [39], [40], ML [41], [42], [43], [44], [45], and tensor networks [46], [47], [48]. The latter include the numerical renormalization group [49], [50], [51], [52], [53], the matrix product state (MPS) [54], [55], [56], [57] as a particular case for 1-D systems, and the density matrix renormalization group [58], [59], [60], [61], [62] as a variational algorithm in the set of MPS [63], [64], [65]. However, perfect or even good models and approximations are not always available or require too much processing capacity, even for today's supercomputers.

Simulating the transport of semiconductor QD systems on classical computers is a demanding task that incorporates phenomena such as Coulomb blockade [1], [66], [67], Pauli spin blockade [68], or sensor dot response [69], for example. Specific models ease the calculation of CSDs [70] that are fundamental for spin-based quantum computation regarding qubit manipulation and information readout.

The constant interaction or capacitance circuit model (CIM) [21], [22], [71], [72] describes the electronic states of QDs and parameterizes the on-site and intersite Coulomb interaction as a network of capacitors, leaking capacitors, and resistors between dots, gates, and leads. It explains many aspects of experiments satisfactorily, but several quantum effects deform the modeled CSDs, sometimes even substantially. Theories capable of considering both classical and quantum effects help to understand the quantum aspects of CSDs and improve their usefulness. The Thomas–Fermi capacitive model (TFCM) of [73] uses the Thomas–Fermi approximation [74] to calculate the electron density of the islands and derive an estimate of inverse capacitive elements for a capacitance model in a given potential profile. It also models the electron transport using a Markov chain among charge states incorporating single electron tunneling rates between islands or to contacts calculated under the Wentzel–Kramers–Brillouin (WKB) tunnel probability [75]. The quantum-mechanical two-level model [76], [77], [78], [79], [80] derives the tunneling of a single electron between two dots from the probability crossover of the two eigenstates, and Zhang et al. [81] investigated its influence on the CSD. The first interest in applying HMs to QD systems appears in the field of collective Coulomb blockade [82], [83]. An effective charge–spin model for QDs [84] based on a lattice description equivalent to a single-band HM incorporated higher order perturbation theory and WKB approximation. Nevertheless, Gaudreau et al. [85], [86] fundamentally demonstrated the capability of HMs to describe CSDs for triple-quantum-dot systems. Later, Yang et al. [87] introduced a generalized HM as the quantum generalization of the classical CIM, including quantum effects such as spin exchange, pair-hopping, and occupation-modulated hopping. Experiments on silicon systems [88] quantitatively confirmed the model's applicability, and the effects of the involved quantum parameters on CSDs have been discussed in depth [89]. To calculate CSDs under a lead bias, Rassekh et al. [90] used Fermi's golden rule to obtain the transition rates, extracted the probabilities of the states, and finally calculated the current. Nevertheless, the generalized HM concentrates on the electronic interaction in the quantum dot system itself and neglects environmental factors [91], [92], [93], [94], [95], [96].

The models often find their application in ML approaches for automated measurement and tuning of QDs. Lennon et al. [97] used the CIM to simulate current maps of single QDs and learned an algorithm that automatically chooses the most informative subsequent measurements. To determine the system's virtual voltages, Oakes et al. [98] applied CIM simulated and experimental CSD data of a 2×2 QD array to train and validate regression models for the extraction of the gradients from a Hough transformation [98]. A purely theoretical approach to CIM simulated data [99] tries to find the most probable convex polytope of Coulomb diamonds in QD measurements by learning a device model using regularized maximum likelihood estimation and 1-D raster scans (rays)

only. Li et al. [100] studied the effects of involved quantum parameters on CSDs of a serial triple QD and confirmed their global features by the similarity between transport measurements and CIM-based simulations. To detect charge states, Darulova et al. [101] evaluated the prediction accuracy of several ML models trained on simulated and experimental data. The simulated data are generated from CIM or taken from the Qflow-lite dataset [102], both improved with five different noise types added. The Qflow-lite dataset is based on the TFCM realization of [73], used to develop deep and convolutional neural networks to tune QD arrays automatically to a double-dot configuration. The dataset intends to provide a reliable dataset of simulated device state (state labels), current, charges, and charge sensor response versus the gate voltages. It extends the TFCM by a charge sensor response. Qflow 2.0 [103] constitutes a further refinement of the dataset by adding synthetic noise characteristic of QD devices. It is part of a framework for robust automated tuning that uses convolutional neural networks for device state estimation and data quality control.

However, implementations of classical simulators for quantum systems are manifold and numerous. Broader application fields are covered, e.g., by QuTiP [104], [105], QuantumATK [106], and Kwant [107], and comprise a set of basic solvers. QuTiP offers solvers for the time evolution of open quantum systems comprising Lindblad master equation (LBMEQ) and MC solvers, routines for the Bloch–Redfield master equation (BRMEQ), periodic systems using the Floquet formalism, and stochastic solvers. Differently, the Kwant Python package provides numerical calculations on tight-binding models (TBMs) with a strong focus on quantum transport. Currently, the Coulomb blockade is not supported directly. QuantumATK offers a fully integrated Python/C++ platform of electronic and atomic-scale modeling tools for electronic structure calculations (via DFT, semiempirical TBM Hamiltonians, and classical and ML force fields) and electron transport simulations (via GF) supporting CSD plots.

Another group of simulators concentrates on the simulation and design of semiconductor-based information devices. The nextnano/nextnano++ [108] 3-D simulator computes electron transport (via SEQ, Poisson equation (PEQ), and current equations) and CSDs for arbitrary designs. The quantum computer-aided design (QCAD) software [109], [110] primarily designs and models silicon multi-QDs developed for qubits. It implements a finite-element method (FEM)-based tool that contains nonlinear PEQ, effective mass SEQ, and configuration interaction solvers. Currently, magnetic fields and direct CSD outputs are not supported. QmeQ [111] focuses on the numerical modeling of stationary-state transport through QD devices (via Pauli MEQ, LBMEQ, Redfield MEQ, and first-order von Neumann approaches) with strong electron–electron interactions. It also computes co-tunneling and pair tunneling [via second-order von Neumann and real-time diagrammatic (RTD)] and broadening of QD states (via RTD), leading to CSDs that include quantum effects. The integrated device simulator for quantum bit design based on impulse technology computer-aided design (TCAD) [112], [113] offers quantum bit output, quantum transport, and qubit operations. The computation pipeline consists of QD potential calculation (via SEQ and PEQ coupled with semiclassical drift diffusion), QD capacitance calculation (via fictitious charge change), micromagnetic simulations (via Ampere's law solved by the finite-volume method), and single-electron quantum transport (via SEQ with magnetic field). Even more focused, quantum-technology computer-aided design (QTCAD) [114] implements an FEM simulator to predict the performance of spin-qubit devices. Incorporated methods include nonlinear PEQ, SEQ, MEQ, and many-body solvers. Quantum transport calculations in the sequential tunneling regime enable the treatment of Coulomb blockade and the calculation of CSDs.

Finally, some simulators only focus on CSD simulation. SIMON [115] simulates single-electron tunnel devices and circuits using the CIM and the MC method for MEQ to implement tunnel junctions. Although designed as a Python-based framework for the tuning and calibration of QDs and spin qubits, QTT [116] offers CIM-based CSD simulation functions. From the system parameters provided, they set up the Hamiltonian, compute the eigenvalues, determine occupation numbers, and finally derive the CSD. Additionally to the CIM-based simulation, the QuDiPy project [117] implements the HM of [88] to generate simulated CSDs.

III. SIMULATION MODEL

Our simulation model combines the simulation of the occupation probabilities (see Section III-A), the sensor response (see Section III-B), and several types of distortions (see Section III-C) into a single framework to provide a comprehensive simulation of CSDs. We conceptualized the handling of the framework to mimic the experiment as well as possible. In particular, we focus on integrating as much flexibility as possible to support different types of dot regimes and charge state tuning experiments. Therefore, the framework enables users:

1) to perform 2-D and 1-D measurements;
2) to measure in different directions with the consideration of the time dependence of certain distortion types;
3) to switch to different sensor configurations, such as for multisensor samples;
4) to switch OFF distortions individually.

All parts of the simulation are interchangeable and defined via simple interfaces, as shown in Fig. 1 .

A. DOT OCCUPATION MODEL

The electron occupation of the dots is the underlying basis for the CSD simulation. Our occupation model is purely geometric and, in contrast to available physical models, provides the flexibility and simplicity to support the different honeycomb shapes we observe in DQD measurements. The fundamental

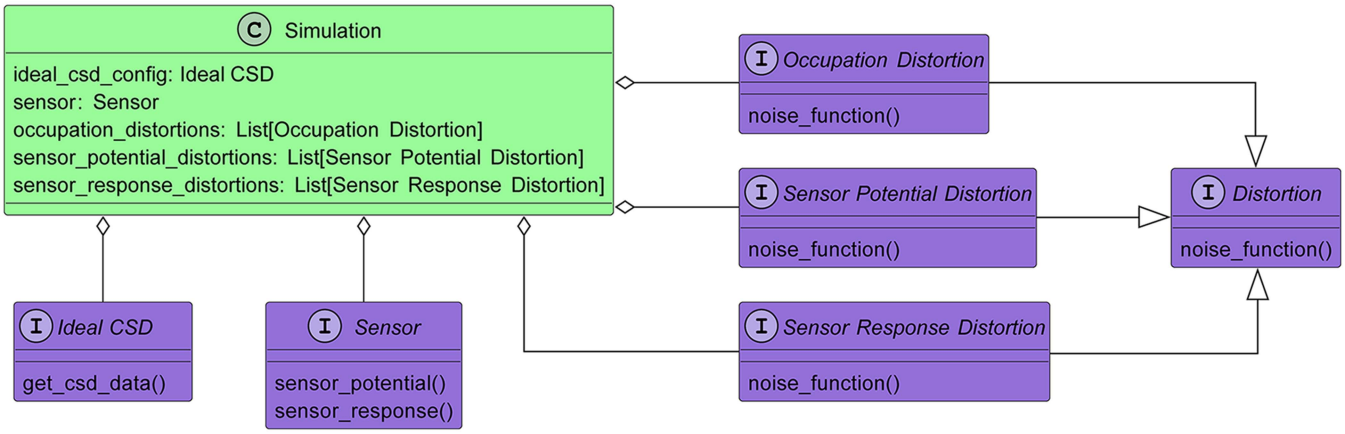

FIGURE 1. Interfaces of the simulation class of our simulation framework. The Python package includes standard implementations.

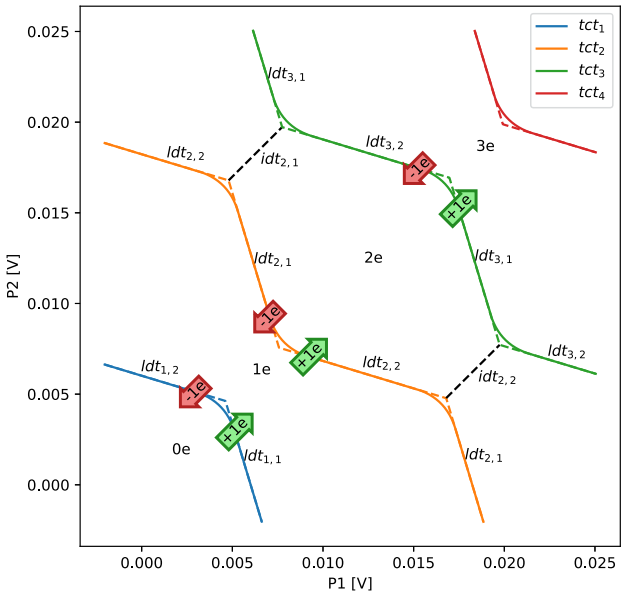

FIGURE 2. Representation of the separation between regions with fixed numbers of electrons using TCTs. The solid lines represent TCTs affected by interdot tunnel coupling, and the dashed lines indicate the LDTs without tunnel coupling.

idea is to describe a CSD as a series of total charge transitions (TCTs) representing the borders between regions containing a fixed number of electrons in the system. Fig. 2 illustrates an example of this representation, where tct_i, $i = 1, \ldots, n$, separates the regions containing $i-1$ and i electrons.

The orientation of the lead-to-dot transitions (LDTs)[2] in the 2-D voltage space depends on the capacitive coupling of the gates. $\mathrm{ldt}_{i,j}$ (associated with tct_i) is primarily affected by plunger gate[3] P_j of qd_j or, in case of using virtual gates,[4] even exclusively by virtual plunger gate P_j^v. For the representation in Fig. 2, $\mathrm{ldt}_{i,1}$ has a slope in the interval $[-\infty, -1)$ ($-\infty$ for virtual gates) and $\mathrm{ldt}_{i,2}$ in the interval $(-1, 0]$ (0 for virtual gates). To mathematically represent the slopes unambiguously, we propose a parametric representation of the TCTs in a voltage space (V'_{P1}, V'_{P2}) originating from (V_{P1}, V_{P2}) by an affine transformation corresponding to a 45° rotation, illustrated in Fig. 3. This results in slope intervals of $[-1, 0)$ for $\mathrm{ldt}_{i,1}$ and $(0, 1]$ for $\mathrm{ldt}_{i,2}$. Depending on the interdot tunnel coupling, the TCT exhibits curves at triple points, where $\mathrm{ldt}_{i,1}$, $\mathrm{ldt}_{i,2}$, and an interdot transition (IDT)[5] intersect. Thus, composing a TCT of linear parts and Bézier curves ensures twice continuous differentiability.

The following parameters define tct_i:

1) $s_{i,j}$: V'_{P1}-intercept of $\mathrm{ldt}_{i,j}$, $(j = 1, 2)$;
2) $m_{i,j}$: slope of $\mathrm{ldt}_{i,j}$, $(j = 1, 2)$;
3) $b_{i,2}$: Bézier anchor on $\mathrm{ldt}_{i,2}$ defining the starting point of the curved part of the first triple point of tct_i;
4) $b_{i,1}$: Bézier anchor on $\mathrm{ldt}_{i,1}$ defining the end point of the curved part of the first triple point of tct_i.

Using only this set of parameters enables the complete construction of a TCT out of repetitions of the linear parts, the Bézier curve, and its 180° rotation. Furthermore, the intersection of the two LDTs constitutes the required center Bézier anchor b_i

$$P1'_{b_i} = \frac{P2'_{b_{i,2}} - P2'_{b_{i,1}} + P1'_{b_{i,1}} \cdot m_{i,1} - P1'_{b_{i,2}} \cdot m_{i,2}}{m_{i,1} - m_{i,2}} \tag{1}$$

$$P2'_{b_i} = P2'_{b_{i,2}} + m_{i,2} \cdot (P1'_{b_i} - P1'_{b_{i,2}}) . \tag{2}$$

The V'_{P1}-intercept of only the linear part is

$$l_{i,j} = s_{i,j} - 2 \cdot |(P1'_{b_{i,j}} - P1'_{b_i})| . \tag{3}$$

Depending on the identifier i of the TCT, the number of Bézier curves and triple points is limited to

$$n_t = 2 \cdot i - 1 . \tag{4}$$

[2] An LDT is a transition where an electron tunnels in (or out) of the dot system from (or to) the leads.

[3] Gates used to primarily control the potential of a dot.

[4] Virtual gates are a linear combination of multiple physical gates used to compensate for capacitive coupling and influence only one parameter of the system.

[5] An IDT describes the tunneling of an electron from one dot to another.

IEEE Transactions on Quantum Engineering

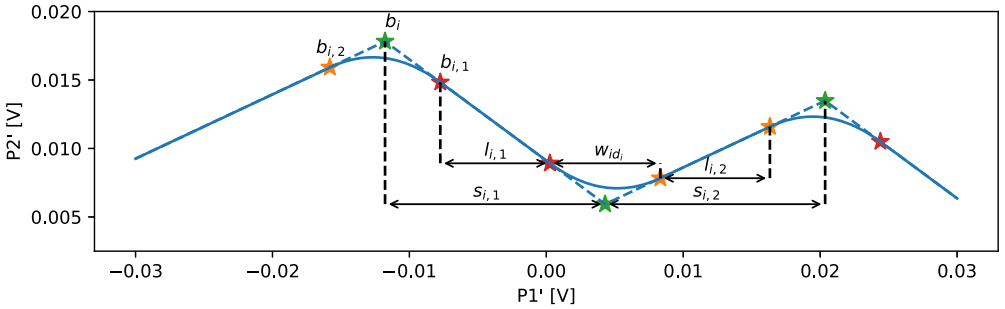

FIGURE 3. TCT description in 1-D (rotated). The blue dashed line represents the TCT without tunnel coupling and the blue solid line with tunnel coupling.

Existing TCTs allow the calculation of the electron occupation. In the area between tct_i and tct_{i+1}, a total of i electrons are in the system. Their distribution to the two QDs qd_1 and qd_2 is determined as follows.

1) The connecting vector from the triple point of tct_i to the opposite triple point of tct_{i+1} represents the IDT $\text{idt}_{i,k}, k \in \{1, \ldots, i\}$.
2) Across each $\text{idt}_{i,k}$, a sigmoid function orthogonal to it approximates the Fermi distribution.
3) The superposition[6] of all sigmoid functions represents the electron occupation of qd_1.
4) The difference between the number of total charges i and the occupation of qd_1 results in the occupation of qd_2.

B. SENSOR MODEL

We calculate the sensor response at each point in the CSD using the simulated occupation information and the sensor characteristic.

Besides the required capacitive coupling of the sensing dot (SD) to the DQD, the SD also cross-couples to the plunger gates of the DQD. In CSDs, the first enables the observation of electron occupation changes as edges, whereas the second appears as undesired value shifts inside the honeycombs.[7] The simulation should incorporate both.

We propose the following model for the sensor response S [118]:

$$\mu_{\text{sd}} = \sum_{j=1}^{2} \left[\alpha_j \cdot N_j + \beta_j \cdot V_{P_j} \right] + \mu_{\text{sd},0}$$

$$S = S_{\text{off}} + a \cdot \frac{\gamma^2}{\gamma^2 + (\mu_{\text{sd}} - \mu_0)^2} \tag{5}$$

where j is the index of the corresponding plunger gate. In this model, μ_{sd} represents the electrochemical potential of the SD influenced by the number of electrons N_j in the dots and the voltages applied to the plunger gates V_{P_j} together with their corresponding lever arms α and β. Effectively, α influences the sharpness of the edges and β the drifts within the honeycombs. Moreover, both effects are counteractive: α is negative, whereas β is positive. Furthermore, the initial potential $\mu_{\text{sd},0}$ of the SD adds to the potential.

A simplified Lorentzian [71] approximates S [Fig. 4(a)]. γ defines its width, and μ_0 the potential at the peak. As linear filters transform the sensor response in the experimental setup, a scaling factor a and an offset S_{off} parameterize the Lorentzian. Fig. 4(b) shows an example of a simulated CSD that includes the cross-coupling effects.

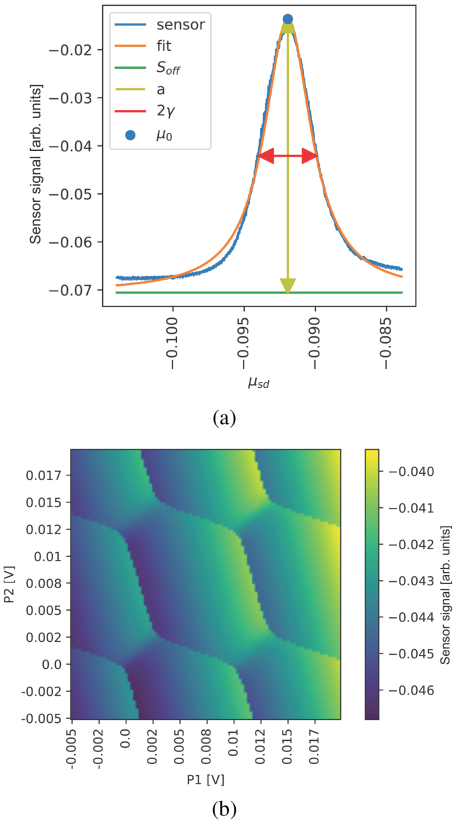

FIGURE 4. Simulation of the sensor response. (a) Measured sensor response (blue) with Lorentzian fit (orange). (b) Example of the sensor response simulated on the left flank of the peak, resulting in rising value shifts with rising voltages in the CSD.

C. DISTORTION MODEL

The simulation of realistic CSDs requires the consideration of occurring distortions [101], [103], [118].

[6] Here, superposition denotes mathematical function combination.

[7] The undesired coupling between the DQD plunger gates and the SD can be compensated by using virtual gates.

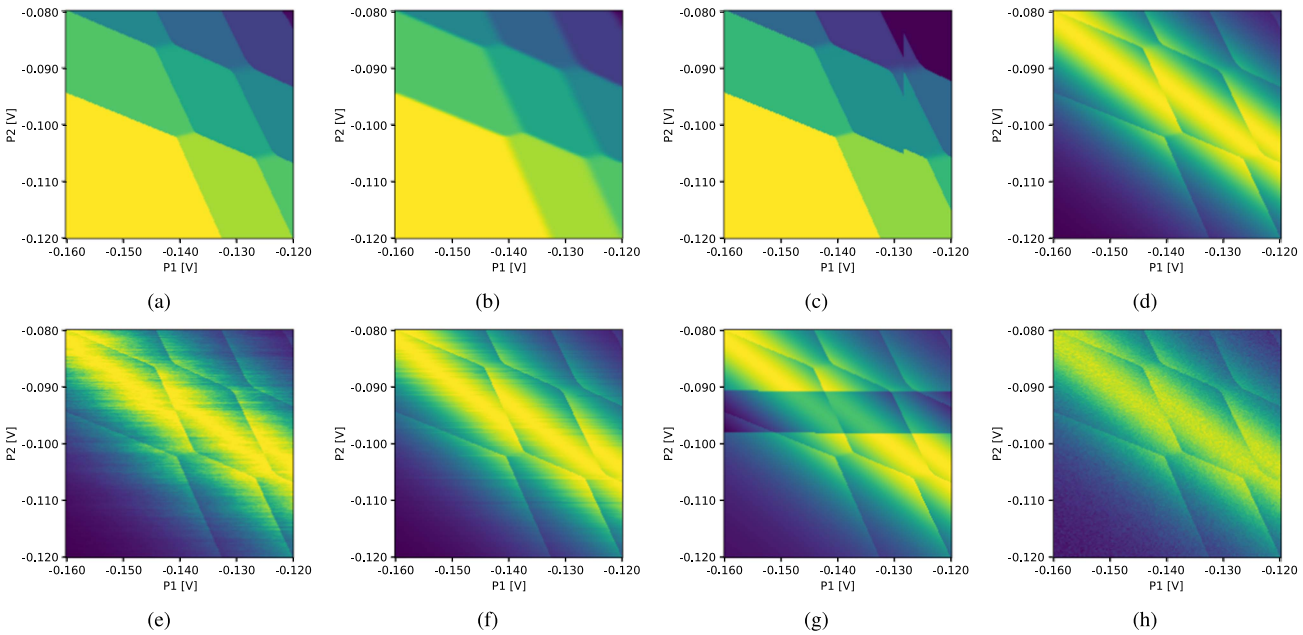

FIGURE 5. Examples of the simulated sensor response and distortions. Distortions affecting the sensor (cat. 2 and 3) are visualized in combination with a sensor response. (a) Ideal CSD. (b) Ideal CSD with occupation transition blurring (cat. 1). (c) Ideal CSD with dot jumps (cat. 1). (d) Ideal CSD with sensor response. (e) Ideal CSD with sensor response and pink noise (cat. 2). (f) Ideal CSD with sensor response and RTN (cat. 2). (g) Ideal CSD with sensor response and RTN (cat. 3). (h) Ideal CSD with sensor response and white noise (cat. 3).

In the following, we define identified distortion phases, assign collected distortion types to these, and describe their sources, simulation, and the required parameters as they typically appear in measurement setups similar to [119], [120]. In addition, we assume samples and their layout to be good enough for scalability (e.g., no spurious QD under the barrier gates or intensively moving QDs), as this is a prerequisite to build a functional quantum computer. Under the assumption that the measurement is performed slow enough, effects like latching can be neglected here.

1) DISTORTION CATEGORIES

We propose to assign the CSD distortions to three categories based on their impact point in the signal path:

1) occupation distortions;
2) SD potential distortions;
3) SD response distortions.

Distortions of the first category alter the simulated occupations of the DQD. The category includes dot jumps (see Section III-C2) and temperature broadening (see Section III-C3).

SD potential distortions comprise random telegraph noise (RTN) (see Section III-C5) and pink noise (see Section III-C4). It is crucial to differentiate these from undesired effects on the nonlinear SD response, primarily white noise (see Section III-C6) and RTN (see Section III-C5).

2) DOT JUMPS

Dot jumps originate from deterministic charge-trapping effects on the QDs caused by fabrication-related imperfections. They become visible as displacements inside the occupation structure of a CSD [103]. We simulate them by shifting a block of columns horizontally, like in Fig. 5(c), or a block of rows vertically.

A geometric distribution of the jump extension simulates their occurrence, whereas a Poisson distribution of the jump amplitude determines their intensity [103].

3) OCCUPATION TRANSITION BLURRING

The thermal occupation of states in the lead reservoir leads to a broadening of the LDTs, which follows the Fermi–Dirac distribution under the assumption that the density of states is constant [121]. We simulate this effect by applying a 1-D Fermi–Dirac filter kernel along the measurement direction.[8]

4) PINK NOISE

Pink noise, also known as $1/f$ or flicker noise, is observed in most electronic devices and results from the internal heterogeneity of electronic components, such as oxide traps or lattice dislocations [122]. Its power spectral density (PSD) is inversely proportional to the frequency and emerges as stripes in linewise measured CSDs.

The generation of pink noise is described in [123] and implemented in the Python module `colorednoise` [124]. In

[8]For the presented results, the Fermi–Dirac filter was still approximated by a Gaussian filter kernel.

our simulation, pink noise is applied to the sensor potential, increasing its visibility in regions with high gradients due to the nonlinear sensor response. The latter corresponds to our observations in experimental data [119].

5) RANDOM TELEGRAPH NOISE

RTN or burst noise randomly switches between two or multiple discrete levels [122]. This effect results from a time-dependent random capture/emission process of charge carriers caused by oxide traps [125]. Its PSD is proportional to $1/f^2$. In linewise measured CSDs, RTN is visible as stripes with a well-defined beginning and ending [see Fig. 5(f)].

We simulate the occurrence of bursts using a geometric distribution for their extension and a normal distribution for their amplitude [103].

Like pink noise, RTN usually appears as noise on the sensor potential. However, the CSDs also contain jumps that affect the sensor response. Therefore, we propose to include RTN additionally in distortion category 3.

6) WHITE NOISE

In the system under consideration, white noise, having a constant PSD characteristic, originates from thermal [126] and shot noise [127]. Thermal noise [126] is caused by the thermal agitation of charge carriers in an electrical conductor, whereas shot noise depends on the discrete charges in the current flow and does not relate to a system's operating temperature.

The amplitude distribution is nearly Gaussian for thermal noise but Poissonian for shot noise. However, as a normal distribution can approximate the Poisson distribution, the simulation combines both noise types into one Gaussian distribution with standard deviation σ_w. In addition, we assume that they solely accrue after the sensor, as their dominating parts result from the amplification of the sensor signal.

IV. PARAMETER EXTRACTION

We exemplarily extracted parameters for the simulation of CSDs from a GaAs sample,[9] which is similar to [129]. Our extraction approach is independent of the sample used.

A. EXTRACTION OF OCCUPATION DATA PARAMETERS

Parameters describing the structure of CSDs can be extracted directly from previously recorded measurements.

Each considered TCT requires the parameters described in Section III-A. We extracted them by manual labeling. It is not necessary to save the parameters for all TCTs. Instead, it is possible to define a transformation rule that generates the next TCT from a previous one, e.g., by shifting the TCT and adjusting w_{id} based on observed relations.

[9]The determined parameters are provided with the simulation software (`default_configs["GaAs_v1"]`) [128].

B. EXTRACTION OF SENSOR PARAMETERS

In our case, the measured sensor scans describe the sensor response as a function of the voltage applied to the plunger gate of the corresponding SD. In addition, we utilize the proportionality of the electrochemical sensor potential to the SD plunger gate in the following.

Fitting the Lorentzian to the experimental sensor scan determines the parameters S_{off}, a, γ, and μ_0 in the sensor model (see Section III-B). For the determination of α_j and β_j, we restrict the following analysis to areas in the CSD with an overall rising value $S(V_{P_1}, V_{P_2})$, corresponding to the left side in the fit $S(\mu_{\text{sd}})$, due to the irreversible uniqueness of the Lorentzian. Then, we can use the inverse fit function $\mu_{\text{sd}}(S)$ to estimate the electrochemical sensor potential $\mu_{\text{sd}}(V_{P_1}, V_{P_2})$. Inside honeycomb regions, we can determine

$$\beta_j = \left(\frac{\partial}{\partial V_{P_j}} \mu_{\text{sd}} \right)_{N_1, N_2 = \text{const}} . \tag{6}$$

Finally, inside the corresponding lead transition areas of the two dots, we calculate

$$\alpha_i = \left(\frac{\Delta(\mu_{\text{sd}}(V_{P_i}) - \beta_i \cdot V_{P_i})}{\Delta N} \right)_{N_i \neq \text{const}, N_{j \neq i} = \text{const}} . \tag{7}$$

C. EXTRACTION OF DISTORTION PARAMETERS

We determine the distortion parameters from different scans. For white noise and RTN of category 3, we use measured CSDs; for pink noise and RTN of category 2, we use sensor scans. However, we characterize dot jumps manually in measured CSDs.

1) DOT JUMPS

There is no method for detecting dot jumps automatically yet. Therefore, we extract the amplitude and extension of the jumps manually. However, as no return is visible in our CSDs, only the intensity of the jumps can be determined. Thus, we assume the extension to be larger than the measured voltage space of the experimental CSDs. Moreover, we extract the parameters for the two swept gates independently, as they might differ depending on the sample.

2) PINK NOISE

The intensity of pink noise in the sensor potential can be determined using the PSD. For this purpose, we examine 2-D sensor scans with a high resolution on the abscissa and a low resolution on the ordinate [119].

However, the sensor potential has to be estimated first. Therefore, for every measured row, a sum of Lorentzians is fitted. If successful[10] for each measured gate voltage, we determine the corresponding sensor potential by computing the inverted Lorentzian of the measurement value.

Now, the PSD of the estimated potential can be determined for every row and averaged over different rows to get a better

[10]evaluated manually; cf. [119].

approximation. To obtain the intensities of the white and pink noise parts, we use the fit from Section IV-C4, because the calculated electrochemical potential includes the white noise from the sensor response. Nevertheless, we extracted the white noise parameters used for the simulation directly from the sensor response.

Tests of our estimation method with simulated data indicate that it usually overestimates the noise by a fixed factor that depends on the Coulomb oscillation characteristics of the sample.

3) RANDOM TELEGRAPH NOISE

Currently, the automatic detection of RTN and the separation from the pink noise in CSDs is problematic. Therefore, we manually investigate sensor scans for RTN of category 2 and determine the bursts' extensions directly and the amplitudes from the jump in the calculated electrochemical sensor potential. Then, the mean of the extensions and the mean and empirical standard deviation of the amplitudes constitute the RTN parameters. Translating the bursts' extension into the CSD domain during the simulation requires considering the measurement time per voltage due to the time-dependent stochastic nature of RTN. We use the median of our CSD measurement time as the default value.

For RTN of category 3, we manually extract the extension and amplitude parameters directly in CSDs. The extension corresponds to the residence time and the amplitude to the observed offset visible in Fig. 5(g).

4) WHITE NOISE

In the PSD of a CSD, white noise dominates in the highest frequencies, while other noise types and the signal itself prevail in lower frequencies. The other types of noise and the signal itself dominate in lower frequencies. The PSD of white noise is given by

$$\mathrm{PSD}_w = c_w \cdot \sigma_w^2. \tag{8}$$

However, as the ratio between pink and white noise varies, we cannot determine a fixed corner frequency for the noise separation. Thus, we fit the sum

$$\mathrm{PSD}_{w,p} = c_w \cdot \sigma_w^2 + \frac{c_p}{f} \cdot \sigma_p^2 \tag{9}$$

of pink and white noise to the highest frequencies of the PSD computed by Welch's method [130][11] from `SciPy` [131]. The fit is applied to the average PSD of all rows to provide a better approximation.

We tested our method with simulated data to study its accuracy. It becomes apparent that it works well for $\sigma_w > 0.001$ and tends to underestimate the intensity of white noise otherwise.

[11] $c_p = 0.1$ and $c_w = 2$ for the Welch method.

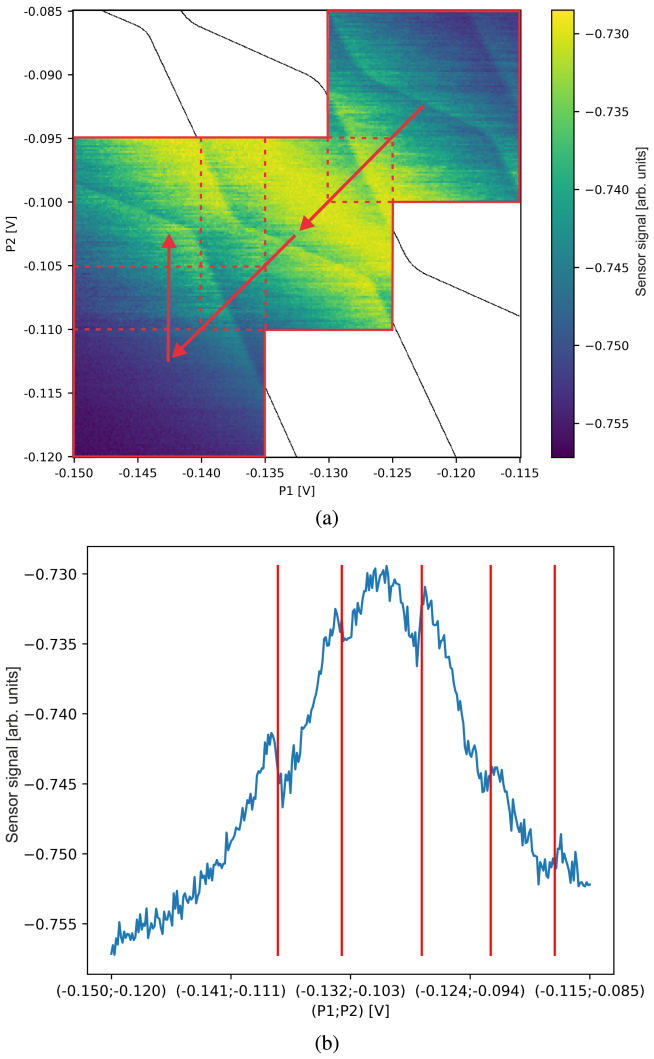

FIGURE 6. Example of simulation results. (a) Simulation of an iterative CSD measurement sequence during tuning. Red boxes illustrate the individually measured CSDs, with the dotted part indicating their overlap and the red arrows their chronological order. (b) Diagonal 1-D scan in the voltage space of (a) with red lines indicating the LDTs.

V. EVALUATION

For assessment, we first visually evaluate our implemented simulation[12] concerning the fidelity, diversity, and plausibility of the generated CSDs. Then, we measure the equivalency to experimental data and, finally, show the performance of our model compared to simulations based on physical models.

A. VISUAL ASSESSMENT

Fig. 6(a) shows an example of a series of 2-D simulations. The structures of the characteristic honeycombs change noticeably over the voltage range, matching the observations from experiments. Also, the distortions and the sensor response resemble the measurements.

[12] We used the configuration `default_configs["GaAs_v1"]` provided in [128], but additionally with varying sensors from [118].

B. METRICS FOR GENERATIVE MODELS

The problem of comparing distributions of generated and measured data also appears in the context of ML when evaluating generative models. However, many of the used metrics in that field, e.g., inception score [132] and Fréchet inception distance [133], are not applicable here because their classification method has to be trained application specific or is pretrained on natural images. Moreover, a metric computed samplewise allows for a better analysis of the simulation model deficiencies. Therefore, we use the α-precision and β-recall metrics to measure the fidelity and diversity of the generated datasets [134]. α-precision describes the probability that a generated sample exists in the α-support of the measured data, whereas β-recall describes the fraction of measured samples that reside in the β-support of the generated data in combination with a chosen k-neighborhood.[13] Both metrics range from zero to one, with high values indicating similar distributions of measured and generated data. Alaa et al. [134] introduced a third metric that indicates if a generative model tends only to copy the training data. This metric is not crucial for our evaluation as we use only the determined parameter ranges for the generation.

To compute the metrics, we first embed the CSDs x_i into a feature hypersphere. Therefore, we use an own adaptation of the `MNIST_LeNet` neural network ϕ implemented in [135]. The training minimizes the loss [136]

$$L = R^2 + \frac{1}{\nu n}\sum_{i=1}^{n}\max\{0, \|\phi(x_i) - c\|^2 - R^2\} \tag{10}$$

where R is the radius of the hypersphere, c represents the center, ν denotes a balancing factor, and n is the number of data points. A corresponding framework for training neural networks is available on GitHub [135].

The selected hyperparameters for the training of the neural network and the computation of the metrics reside in [118].

1) PREPROCESSING AND TRAINING

Before applying the neural network, a normalization aligns the different value ranges of the CSDs.

We train the network with randomly selected 50% of the available 484 experimental datasets, with the other 50% constituting the test set. In order to increase the amount of data during training, we apply rotations, flips, and random brightness and contrast changes to the CSDs using the Python package `albumentations` [137].

2) RESULTS

For the result investigation, our simulation should include only all outliers represented in the experimental data. Thus, we set the parameters α and β to 1, to calculate the results depicted in Table 1. Then, we test whether our network can embed CSDs into a feature hypersphere that sufficiently distinguishes CSDs from non-CSD data. Therefore, we benchmark the training set against the retained experimental test set. It achieves high precision and recall values, indicating a reasonable mapping. For the k-nearest-neighbor region, we find $k = 9$ as the minimum, leading to a recall of 100% in our data [134].

TABLE 1. Evaluation Results Utilizing 1-Precision and 1-Recall

Dataset	1-precision [%]	1-recall (k = 9) [%]
Experimental training set	98.8	100.0
MNIST	100.0	2.5
MNIST expanded	100.0	3.3
SimCATS	99.6	67.5
SimCATS expanded	99.8	79.0

We compare the listed datasets to the experimental data test set. The datasets MNIST and SimCATS contain the same number of images as the experimental test set. Additionally, we supply results for expanded MNIST and SimCATS datasets with roughly ten times the size of the test set.

Furthermore, we test whether the network embeds non-CSD data into the same hypersphere. Tests with MNIST data[14] [138] achieve a high precision but a very low recall, indicating that they occupy a noncoinciding subspace. In conclusion, our network can map CSD data into an appropriate feature hypersphere, and the applied metrics are suitable to evaluate the equivalency of experimental and simulated CSDs.

The metrics result in a high precision and a recall of 67.5%. In contrast to the simulated data, we must consider that the experimental data do not cover the whole voltage space homogeneously but prefer particular regions due to the experimenter's experience. A comparison with about ten times the amount of data increases the recall to 79.0%, which supports our hypothesis. In contrast, using ten times more MNIST data than experimental CSDs does not significantly increase the recall.

In summary, the simulated data align strongly with the experimental data and map their distribution to a large extent. Nevertheless, the results indicate that our simulation does not yet represent all experimental CSDs. As some of the available experimental datasets include anomalies from postprocessing steps not represented in our simulation, we expect an even higher coverage for unprocessed data.

C. PERFORMANCE ANALYSIS

We benchmark the geometric simulation approach against two typical physical simulations regarding the execution time per simulation using an Intel Xeon w5-2455X—3.19 GHz. For the comparison, we configure the parameters of the different approaches so that the simulated area covers similar structures. Then, we perform simulations of different resolutions and average the execution time over 50 runs each. Fig. 7 visualizes the results. It is noticeable that the execution time

[13] α- or β-support is the minimum volume (sphere) subset of the whole set that supports a probability mass of α or β.

[14] The MNIST dataset consists of images containing handwritten digits.

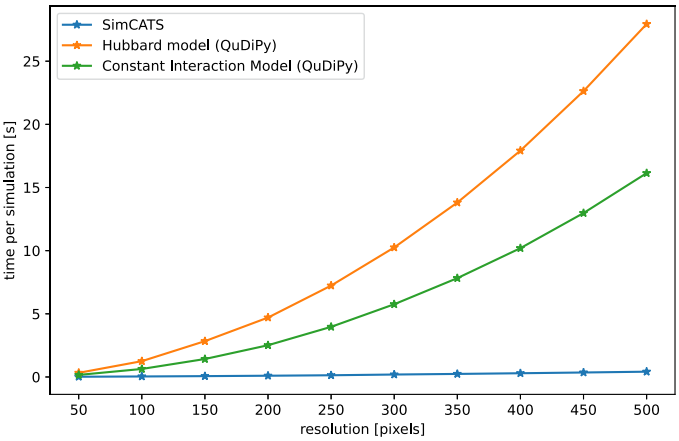

FIGURE 7. Average execution time of different simulation approaches in dependence on the resolution (in pixels per axis). The time refers to the computation per CSD (without distortions) after the previous initialization. Physical simulation models implemented in QuDiPy [117] show a quadratic time performance, while SimCATS hardly depends on the image resolution.

of the physical models increases quadratically with the resolution per axis. Furthermore, the HM, which includes quantum effects like tunnel coupling, is significantly slower than the constant interaction model. In comparison, the execution time for the geometric model is always lower[15] and hardly increases because the computation of TCTs is the decisive factor here, whereas the calculation of pixels is very fast.

VI. CONCLUSION

In this article, we presented an approach for the simulation of CSD data, which incorporates the most relevant effects observed in measurements. First, we defined our model, comprising the ideal data generation, the sensor reaction, and distortions. Our TCT-based geometric representation of CSD structures enables the ideal data simulation for DQDs, independent of the sample material and layout. Furthermore, the sensor model includes the representation of observed Coulomb peaks as simplified Lorentzians and the sensor potential's dependence on lever arms of the DQD's gate voltages and occupation. Considering a typical measurement signal path, we assigned the distortions to three newly proposed categories and defined their source, simulation, and parameters afterward. Next, we extracted the different model parameters from measured data and, finally, showed simulation results and analyzed the capabilities of the simulation to mimic a diverse set of measured data.

We suggest using our simulation framework for tuning algorithm development and benchmarking. It generates realistic data, allows a quick generation of large datasets with known ground truth, and enables fair comparability of diverse approaches of different sites. With complete control over the strength of the distortions and the sensitivity of the sensor, it additionally enables the determination of minimum measurement requirements for the success of an algorithm. Furthermore, using the provided interfaces, our open-source Python framework is designed for simple extension and adaptation. Thus, we highly encourage the contributions of other groups to build up a standard framework that drives the development of automated tuning solutions.

Future work on our CSD simulation could incorporate further effects and their influence on the data. For example, computing wider CSD scans[16] can incorporate the varying lengths of the LDTs. The correlation between consecutively recorded CSDs or multiple DQDs measured at the same time are of minor impact but can be included if required. Another open question addresses the relationship between the geometric TCT parameters and the parameters of physical models. With such knowledge, the simulation can directly adapt the geometric parameters to changes in the system. Thus, our fast simulation approach can support the development of more complex tuning routines. Furthermore, algorithms only trained on simulated data must be tested in experiments, and parameter sets by other sites' experiments are necessary to develop and benchmark robust technology-independent algorithms.

ACKNOWLEDGMENT

The authors appreciate helpful discussions with Jan-Oliver Kropp on evaluation metrics for generative models.

REFERENCES

[1] H. Grabert and M. H. Devoret, Eds., *Single Charge Tunneling: Coulomb Blockade Phenomena In Nanostructures* (NATO ASI Series), vol. 294. Boston, MA, USA: Springer, 1992, doi: 10.1007/978-1-4757-2166-9.

[2] Y. V. Nazarov, "Quantum interference, tunnel junctions and resonant tunneling interferometer," *Phys. B: Condens. Matter*, vol. 189, no. 1, pp. 57–69, Jun. 1993, doi: 10.1016/0921-4526(93)90146-W.

[3] J. König, J. Schmid, H. Schoeller, and G. Schön, "Resonant tunneling through ultrasmall quantum dots: Zero-bias anomalies, magnetic-field dependence, and boson-assisted transport," *Phys. Rev. B*, vol. 54, no. 23, pp. 16820–16837, Dec. 1996, doi: 10.1103/PhysRevB.54.16820.

[4] C. Timm, "Tunneling through molecules and quantum dots: Master-equation approaches," *Phys. Rev. B*, vol. 77, no. 19, May 2008, Art. no. 195416, doi: 10.1103/PhysRevB.77.195416.

[5] R. P. Feynman and F. L. Vernon, "The theory of a general quantum system interacting with a linear dissipative system," *Ann. Phys.*, vol. 24, pp. 118–173, Oct. 1963, doi: 10.1016/0003-4916(63)90068-X.

[6] D. J. Singh, "Overview of density functional theory and methods," in *Planewaves, Pseudopotentials and the LAPW Method*, D. J. Singh, Ed., Boston, MA, USA: Springer, 1994, pp. 5–16, doi: 10.1007/978-1-4757-2312-0_2.

[7] F. Siano and R. Egger, "Josephson current through a nanoscale magnetic quantum dot," *Phys. Rev. Lett.*, vol. 93, no. 4, Jul. 2004, Art. no. 0047002, doi: 10.1103/PhysRevLett.93.047002.

[8] V. Pokorný and M. Žonda, "Correlation effects in superconducting quantum dot systems," *Phys. B: Condens. Matter*, vol. 536, pp. 488–491, May 2018, doi: 10.1016/j.physb.2017.08.059.

[9] K. Hepp, "The classical limit for quantum mechanical correlation functions," *Commun. Math. Phys.*, vol. 35, no. 4, pp. 265–277, Dec. 1974, doi: 10.1007/BF01646348.

[15] For the resolutions in [50, 500], the execution time is in [19, 418] ms with a memory requirement in [44.4, 90.0] MB.

[16] For applications that analyze only small voltage ranges, we do not consider this to be necessary.

[10] J. Ginibre and G. Velo, "The classical field limit of scattering theory for non-relativistic many-boson systems. II," *Commun. Math. Phys.*, vol. 68, no. 1, pp. 45–68, Feb. 1979, doi: 10.1007/BF01562541.

[11] L. Erdos and H.-T. Yau, "Derivation of the nonlinebar Schrödinger equation from a many-body Coulomb system," *Adv. Theor. Math. Phys.*, vol. 5, no. 6, pp. 1169–1205, 2001, doi: 10.4310/ATMP.2001.v5.n6.a6.

[12] B. R. Bułka and T. Kostyrko, "Electronic correlations in coherent transport through a two quantum dot system," *Phys. Rev. B*, vol. 70, no. 20, Nov. 2004, Art. no. 205333, doi: 10.1103/PhysRevB.70.205333.

[13] D. Sztenkiel and R. Świrkowicz, "Electron transport through double quantum dot system with inter-dot coulomb interaction," *Acta Phys. Polonica A*, vol. 111, no. 3, pp. 361–372, Mar. 2007, doi: 10.12693/APhysPolA.111.361.

[14] A. Zagoskin, *Quantum Theory of Many-Body Systems: Techniques and Applications* (ser. Graduate Texts in Physics). Cham, Switzerland: Springer, 2014, doi: 10.1007/978-3-319-07049-0.

[15] T. A. Brody, J. Flores, J. B. French, P. A. Mello, A. Pandey, and S. S. M. Wong, "Random-matrix physics: Spectrum and strength fluctuations," *Rev. Modern Phys.*, vol. 53, no. 3, pp. 385–479, Jul. 1981, doi: 10.1103/RevModPhys.53.385.

[16] R. G. Newton, *Scattering Theory of Waves and Particles*. Berlin, Germany: Springer, 1982, doi: 10.1007/978-3-642-88128-2.

[17] C. W. J. Beenakker, "Random-matrix theory of quantum transport," *Rev. Modern Phys.*, vol. 69, no. 3, pp. 731–808, Jul. 1997, doi: 10.1103/RevModPhys.69.731.

[18] W. Pötz, "Scattering approach to semiconductor double quantum dot cavities," *Phys. Rev. B*, vol. 77, no. 3, Jan. 2008, Art. no. 35310, doi: 10.1103/PhysRevB.77.035310.

[19] R. P. Feynman, "Simulating physics with computers," *Int. J. Theor. Phys.*, vol. 21, no. 6, pp. 467–488, Jun. 1982, doi: 10.1007/BF02650179.

[20] I. M. Georgescu, S. Ashhab, and F. Nori, "Quantum simulation," *Rev. Modern Phys.*, vol. 86, no. 1, pp. 153–185, Mar. 2014, doi: 10.1103/RevModPhys.86.153.

[21] W. G. van der Wiel, S. De Franceschi, J. M. Elzerman, T. Fujisawa, S. Tarucha, and L. P. Kouwenhoven, "Electron transport through double quantum dots," *Rev. Modern Phys.*, vol. 75, no. 1, pp. 1–22, Dec. 2002, doi: 10.1103/RevModPhys.75.1.

[22] R. Hanson, L. P. Kouwenhoven, J. R. Petta, S. Tarucha, and L. M. K. Vandersypen, "Spins in few-electron quantum dots," *Rev. Modern Phys.*, vol. 79, no. 4, pp. 1217–1265, Oct. 2007, doi: 10.1103/RevModPhys.79.1217.

[23] P. Barthelemy and L. M. K. Vandersypen, "Quantum dot systems: A versatile platform for quantum simulations," *Ann. Phys.*, vol. 525, nos. 10/11, pp. 808–826, Nov. 2013, doi: 10.1002/andp.201300124.

[24] T. Byrnes, N. Y. Kim, K. Kusudo, and Y. Yamamoto, "Quantum simulation of Fermi-Hubbard models in semiconductor quantum-dot arrays," *Phys. Rev. B*, vol. 78, no. 7, Aug. 2008, Art. no. 075320, doi: 10.1103/PhysRevB.78.075320.

[25] T. Hensgens et al., "Quantum simulation of a Fermi-Hubbard model using a semiconductor quantum dot array," *Nature*, vol. 548, no. 7665, pp. 70–73, Aug. 2017, doi: 10.1038/nature23022.

[26] T. Hensgens, "Emulating Fermi-Hubbard physics with quantum dots: From few to more and how to," Ph.D. dissertation, QuTech Adv. Res. Centre, Delft Univ. Technol., Delft, The Netherlands, 2018, doi: 10.4233/uuid:b71f3b0b-73a0-4996-896c-84ed43e72035.

[27] X. Wang et al., "Experimental realization of an extended fermi-Hubbard model using a 2D lattice of dopant-based quantum dots," *Nature Commun.*, vol. 13, no. 1, Nov. 2022, Art. no. 6824, doi: 10.1038/s41467-022-34220-w.

[28] J. P. Dehollain et al., "Nagaoka ferromagnetism observed in a quantum dot plaquette," *Nature*, vol. 579, no. 7800, pp. 528–533, Mar. 2020, doi: 10.1038/s41586-020-2051-0.

[29] C. van Diepen, "Quantum simulation with electron spins in quantum dots," Ph.D. dissertation, QuTech Adv. Res. Centre, Delft Univ. Technol., Delft, The Netherlands, 2021, doi: 10.4233/uuid:f7adb947-1d56-4326-aa99-13b5baa353f6.

[30] C. J. van Diepen, T.-K. Hsiao, U. Mukhopadhyay, C. Reichl, W. Wegscheider, and L. M. K. Vandersypen, "Quantum simulation of antiferromagnetic Heisenberg chain with gate-defined quantum dots," *Phys. Rev. X*, vol. 11, no. 4, Nov. 2021, Art. no. 041025, doi: 10.1103/PhysRevX.11.041025.

[31] M. Suzuki, *Quantum Monte Carlo Methods in Condensed Matter Physics*. Singapore: World Scientific, Dec. 1993, doi: 10.1142/2262.

[32] D. J. Luitz and F. F. Assaad, "Weak-coupling continuous-time quantum Monte Carlo study of the single impurity and periodic Anderson models with *s*-wave superconducting baths," *Phys. Rev. B*, vol. 81, no. 2, Jan. 2010, Art. no. 024509, doi: 10.1103/PhysRevB.81.024509.

[33] R. M. Dreizler and E. K.U. Gross, "Many-body perturbation theory," in *Density Functional Theory: An Approach to the Quantum Many-Body Problem*, R. M. Dreizler and E. K. U. Gross, Eds., Berlin, Germany: Springer, 1990, pp. 138–172, doi: 10.1007/978-3-642-86105-5_6.

[34] A. L. Fetter and J. D. Walecka, *Quantum Theory of Many-Particle Systems*. North Chelmsford, MA, USA: Courier Corporation, Jun. 2003.

[35] H. D. Meyer, U. Manthe, and L. S. Cederbaum, "The multi-configurational time-dependent Hartree approach," *Chem. Phys. Lett.*, vol. 165, no. 1, pp. 73–78, Jan. 1990, doi: 10.1016/0009-2614(90)87014-I.

[36] U. Manthe, H.-D. Meyer, and L. S. Cederbaum, "Wave-packet dynamics within the multiconfiguration Hartree framework: General aspects and application to NOCl," *J. Chem. Phys.*, vol. 97, no. 5, pp. 3199–3213, Sep. 1992, doi: 10.1063/1.463007.

[37] M. H. Beck, A. Jäckle, G. A. Worth, and H. D. Meyer, "The multiconfiguration time-dependent Hartree (MCTDH) method: A highly efficient algorithm for propagating wavepackets," *Phys. Rep.*, vol. 324, no. 1, pp. 1–105, Jan. 2000, doi: 10.1016/S0370-1573(99)00047-2.

[38] Y. Tanimura and R. Kubo, "Time evolution of a quantum system in contact with a nearly Gaussian-Markoffian noise bath," *J. Phys. Soc. Jpn.*, vol. 58, no. 1, pp. 101–114, Jan. 1989, doi: 10.1143/JPSJ.58.101.

[39] Y. Tanimura, "Nonperturbative expansion method for a quantum system coupled to a harmonic-oscillator bath," *Phys. Rev. A*, vol. 41, no. 12, pp. 6676–6687, Jun. 1990, doi: 10.1103/PhysRevA.41.6676.

[40] Y. Tanimura, "Equation approaches to quantum dissipative systems," *J. Phys. Soc. Jpn.*, vol. 75, no. 8, Aug. 2006, Art. no. 082001, doi: 10.1143/JPSJ.75.082001.

[41] G. Carleo and M. Troyer, "Solving the quantum many-body problem with artificial neural networks," *Science*, vol. 355, no. 6325, pp. 602–606, Feb. 2017, doi: 10.1126/science.aag2302.

[42] M. J. Hartmann and G. Carleo, "Neural-network approach to dissipative quantum many-body dynamics," *Phys. Rev. Lett.*, vol. 122, no. 25, Jun. 2019, Art. no. 250502, doi: 10.1103/PhysRevLett.122.250502.

[43] K. T. Schütt, M. Gastegger, A. Tkatchenko, K.-R. Müller, and R. J. Maurer, "Unifying machine learning and quantum chemistry with a deep neural network for molecular wavefunctions," *Nature Commun.*, vol. 10, no. 1, Nov. 2019, Art. no. 5024, doi: 10.1038/s41467-019-12875-2.

[44] J. Hermann, Z. Schätzle, and F. Noé, "Deep-neural-network solution of the electronic Schrödinger equation," *Nature Chem.*, vol. 12, no. 10, pp. 891–897, Oct. 2020, doi: 10.1038/s41557-020-0544-y.

[45] S. Manzhos, "Machine learning for the solution of the Schrödinger equation," *Mach. Learn., Sci. Technol.*, vol. 1, no. 1, Apr. 2020, Art. no. 013002, doi: 10.1088/2632-2153/ab7d30.

[46] G. Vidal, "Efficient simulation of one-dimensional quantum many-body systems," *Phys. Rev. Lett.*, vol. 93, no. 4, Jul. 2004, Art. no. 040502, doi: 10.1103/PhysRevLett.93.040502.

[47] R. Hong, Y.-X. Xiao, J. Hu, A.-C. Ji, and S.-J. Ran, "Functional tensor network solving many-body Schrödinger equation," *Phys. Rev. B*, vol. 105, no. 16, Apr. 2022, Art. no. 165116, doi: 10.1103/PhysRevB.105.165116.

[48] R. Orús, "Tensor networks for complex quantum systems," *Nature Rev. Phys.*, vol. 1, no. 9, pp. 538–550, Sep. 2019, doi: 10.1038/s42254-019-0086-7.

[49] K. G. Wilson, "The renormalization group: Critical phenomena and the Kondo problem," *Rev. Modern Phys.*, vol. 47, no. 4, pp. 773–840, Oct. 1975, doi: 10.1103/RevModPhys.47.773.

[50] T. Yoshioka and Y. Ohashi, "Numerical renormalization group studies on single impurity Anderson model in superconductivity: A unified treatment of magnetic, nonmagnetic impurities, and resonance scattering," *J. Phys. Soc. Jpn.*, vol. 69, no. 6, pp. 1812–1823, Jun. 2000, doi: 10.1143/JPSJ.69.1812.

[51] A. Oguri, Y. Tanaka, and A. C. Hewson, "Quantum phase transition in a minimal model for the Kondo effect in a Josephson junction," *J. Phys. Soc. Jpn.*, vol. 73, no. 9, pp. 2494–2504, Sep. 2004, doi: 10.1143/JPSJ.73.2494.

[52] R. Bulla, T. A. Costi, and T. Pruschke, "Numerical renormalization group method for quantum impurity systems," *Rev. Modern Phys.*, vol. 80, no. 2, pp. 395–450, Apr. 2008, doi: 10.1103/RevModPhys.80.395.

[53] A. Oguri, Y. Tanaka, and J. Bauer, "Interplay between Kondo and Andreev-Josephson effects in a quantum dot coupled to one normal and two superconducting leads," *Phys. Rev. B*, vol. 87, no. 7, Feb. 2013, Art. no. 075432, doi: 10.1103/PhysRevB.87.075432.

[54] M. Fannes, B. Nachtergaele, and R. F. Werner, "Finitely correlated states on quantum spin chains," *Commun. Math. Phys.*, vol. 144, no. 3, pp. 443–490, Mar. 1992, doi: 10.1007/BF02099178.

[55] G. Vidal, "Efficient classical simulation of slightly entangled quantum computations," *Phys. Rev. Lett.*, vol. 91, no. 14, Oct. 2003, Art. no. 147902, doi: 10.1103/PhysRevLett.91.147902.

[56] F. Verstraete, V. Murg, and J. Cirac, "Matrix product states, projected entangled pair states, and variational renormalization group methods for quantum spin systems," *Adv. Phys.*, vol. 57, no. 2, pp. 143–224, Mar. 2008, doi: 10.1080/14789940801912366.

[57] I. Cirac, D. Perez-Garcia, N. Schuch, and F. Verstraete, "Matrix product states and projected entangled pair states: Concepts, symmetries, and theorems," *Rev. Modern Phys.*, vol. 93, no. 4, Dec. 2021, Art. no. 045003, doi: 10.1103/RevModPhys.93.045003.

[58] S. R. White, "Density matrix formulation for quantum renormalization groups," *Phys. Rev. Lett.*, vol. 69, no. 19, pp. 2863–2866, Nov. 1992, doi: 10.1103/PhysRevLett.69.2863.

[59] S. R. White, "Density-matrix algorithms for quantum renormalization groups," *Phys. Rev. B*, vol. 48, no. 14, pp. 10345–10356, Oct. 1993, doi: 10.1103/PhysRevB.48.10345.

[60] H. Takasaki, T. Hikihara, and T. Nishino, "Fixed point of the finite system DMRG," *J. Phys. Soc. Jpn.*, vol. 68, no. 5, pp. 1537–1540, May 1999, doi: 10.1143/JPSJ.68.1537.

[61] U. Schollwöck, "The density-matrix renormalization group," *Rev. Modern Phys.*, vol. 77, no. 1, pp. 259–315, Apr. 2005, doi: 10.1103/RevModPhys.77.259.

[62] U. Schollwöck, "The density-matrix renormalization group in the age of matrix product states," *Ann. Phys.*, vol. 326, no. 1, pp. 96–192, Jan. 2011, doi: 10.1016/j.aop.2010.09.012.

[63] S. östlund and S. Rommer, "Thermodynamic limit of density matrix renormalization," *Phys. Rev. Lett.*, vol. 75, no. 19, pp. 3537–3540, Nov. 1995, doi: 10.1103/PhysRevLett.75.3537.

[64] J. Dukelsky, M. A. Martín-Delgado, T. Nishino, and G. Sierra, "Equivalence of the variational matrix product method and the density matrix renormalization group applied to spin chains," *Europhys. Lett.*, vol. 43, no. 4, Aug. 1998, Art. no. 457, doi: 10.1209/epl/i1998-00381-x.

[65] F. Verstraete, D. Porras, and J. I. Cirac, "Density matrix renormalization group and periodic boundary conditions: A quantum information perspective," *Phys. Rev. Lett.*, vol. 93, no. 22, Nov. 2004, Art. no. 227205, doi: 10.1103/PhysRevLett.93.227205.

[66] C. W. J. Beenakker, "Theory of coulomb-blockade oscillations in the conductance of a quantum dot," *Phys. Rev. B*, vol. 44, no. 4, pp. 1646–1656, Jul. 1991, doi: 10.1103/PhysRevB.44.1646.

[67] C. Livermore, C. H. Crouch, R. M. Westervelt, K. L. Campman, and A. C. Gossard, "The Coulomb blockade in coupled quantum dots," *Science*, vol. 274, no. 5291, pp. 1332–1335, Nov. 1996, doi: 10.1126/science.274.5291.1332.

[68] K. Ono, D. G. Austing, Y. Tokura, and S. Tarucha, "Current rectification by Pauli exclusion in a weakly coupled double quantum dot system," *Science*, vol. 297, no. 5585, pp. 1313–1317, Aug. 2002, doi: 10.1126/science.1070958.

[69] J. M. Elzerman et al., "Few-electron quantum dot circuit with integrated charge read out," *Phys. Rev. B*, vol. 67, no. 16, Apr. 2003, Art. no. 161308, doi: 10.1103/PhysRevB.67.161308.

[70] F. Hofmann et al., "Single electron switching in a parallel quantum dot," *Phys. Rev. B*, vol. 51, no. 19, pp. 13872–13875, May 1995, doi: 10.1103/PhysRevB.51.13872.

[71] L. P. Kouwenhoven, C. M. Marcus, P. L. McEuen, S. Tarucha, R. M. Westervelt, and N. S. Wingreen, "Electron transport in quantum dots," in *Mesoscopic Electron Transport*, L. L. Sohn, L. P. Kouwenhoven, and G. Schön, Eds., Dordrecht, The Netherlands: Springer. 1997, pp. 105–214, doi: 10.1007/978-94-015-8839-3_4.

[72] D. Schröer et al., "Electrostatically defined serial triple quantum dot charged with few electrons," *Phys. Rev. B*, vol. 76, no. 7, Aug. 2007, Art. no. 075306, doi: 10.1103/PhysRevB.76.075306.

[73] S. S. Kalantre et al., "Machine learning techniques for state recognition and auto-tuning in quantum dots," *Npj Quantum Inf.*, vol. 5, no. 1, Dec. 2019, Art. no. 6, doi: 10.1038/s41534-018-0118-7.

[74] N. H. March, "Origins—The Thomas-Fermi Theory," in *Theory of the Inhomogeneous Electron Gas* (ser. Physics of Solids and Liquids), S. Lundqvist and N. H. March, Eds., Boston, MA, USA: Springer, 1983, pp. 1–77, doi: 10.1007/978-1-4899-0415-7_1.

[75] E. Merzbacher, *Quantum Mechanics*. Hoboken, NJ, USA: Wiley, 1998.

[76] L. DiCarlo et al., "Differential charge sensing and charge delocalization in a tunable double quantum dot," *Phys. Rev. Lett.*, vol. 92, no. 22, Jun. 2004, Art. no. 226801, doi: 10.1103/PhysRevLett.92.226801.

[77] J. R. Petta, A. C. Johnson, C. M. Marcus, M. P. Hanson, and A. C. Gossard, "Manipulation of a single charge in a double quantum dot," *Phys. Rev. Lett.*, vol. 93, no. 18, Art. no. 186802, Oct. 2004, doi: 10.1103/PhysRevLett.93.186802.

[78] T. Hatano, M. Stopa, and S. Tarucha, "Single-electron delocalization in hybrid vertical-lateral double quantum dots," *Science*, vol. 309, no. 5732, pp. 268–271, Jul. 2005, doi: 10.1126/science.1111205.

[79] A. K. Hüttel, S. Ludwig, H. Lorenz, K. Eberl, and J. P. Kotthaus, "Direct control of the tunnel splitting in a one-electron double quantum dot," *Phys. Rev. B*, vol. 72, no. 8, Aug. 2005, Art. no. 081310, doi: 10.1103/PhysRevB.72.081310.

[80] M. Pioro-Ladriére et al., "Charge sensing of an artificial $\{H\}^{\{+\}}_{\{2\}}$ molecule in lateral quantum dots," *Phys. Rev. B*, vol. 72, no. 12, Sep. 2005, Art. no. 125307, doi: 10.1103/PhysRevB.72.125307.

[81] L.-X. Zhang, D. V. Melnikov, and J.-P. Leburton, "Exchange interaction and stability diagram of coupled quantum dots in magnetic fields," *Phys. Rev. B*, vol. 74, no. 20, Nov. 2006, Art. no. 205306, doi: 10.1103/PhysRevB.74.205306.

[82] C. A. Stafford and S. Das Sarma, "Collective coulomb blockade in an array of quantum dots: A Mott-Hubbard approach," *Phys. Rev. Lett.*, vol. 72, no. 22, pp. 3590–3593, May 1994, doi: 10.1103/PhysRevLett.72.3590.

[83] R. Kotlyar, C. A. Stafford, and S. Das Sarma, "Correlated charge polarization in a chain of coupled quantum dots," *Phys. Rev. B*, vol. 58, no. 4, pp. R1746–R1749, Jul. 1998, doi: 10.1103/PhysRevB.58.R1746.

[84] J. H. Jefferson and W. Häusler, "Effective charge-spin models for quantum dots," *Phys. Rev. B*, vol. 54, no. 7, pp. 4936–4947, Aug. 1996, doi: 10.1103/PhysRevB.54.4936.

[85] L. Gaudreau et al., "Stability diagram of a few-electron triple dot," *Phys. Rev. Lett.*, vol. 97, no. 3, Jul. 2006, Art. no. 036807, doi: 10.1103/PhysRevLett.97.036807.

[86] M. Korkusinski, I. P. Gimenez, P. Hawrylak, L. Gaudreau, S. A. Studenikin, and A. S. Sachrajda, "Topological Hunds rules and the electronic properties of a triple lateral quantum dot molecule," *Phys. Rev. B*, vol. 75, no. 11, Mar. 2007, Art. no. 115301, doi: 10.1103/PhysRevB.75.115301.

[87] S. Yang, X. Wang, and S. Das Sarma, "Generic Hubbard model description of semiconductor quantum-dot spin qubits," *Phys. Rev. B*, vol. 83, no. 16, Apr. 2011, Art. no. 161301, doi: 10.1103/PhysRevB.83.161301.

[88] S. Das Sarma, X. Wang, and S. Yang, "Hubbard model description of silicon spin qubits: Charge stability diagram and tunnel coupling in Si double quantum dots," *Phys. Rev. B*, vol. 83, no. 23, Jun. 2011, Art. no. 235314, doi: 10.1103/PhysRevB.83.235314.

[89] X. Wang, S. Yang, and S. Das Sarma, "Quantum theory of the charge-stability diagram of semiconductor double-quantum-dot systems," *Phys. Rev. B*, vol. 84, no. 11, Sep. 2011, Art. no. 115301, doi: 10.1103/PhysRevB.84.115301.

[90] A. Rassekh, M. Shalchian, J.-M. Sallese, and F. Jazaeri, "Tunneling current through a double quantum dots system," *IEEE Access*, vol. 10, pp. 75245–75256, 2022, doi: 10.1109/ACCESS.2022.3190617.

[91] M. J. Storcz, U. Hartmann, S. Kohler, and F. K. Wilhelm, "Intrinsic phonon decoherence and quantum gates in coupled lateral quantum-dot charge qubits," *Phys. Rev. B*, vol. 72, no. 23, Dec. 2005, Art. no. 235321, doi: 10.1103/PhysRevB.72.235321.

[92] V. N. Stavrou and X. Hu, "Charge decoherence in laterally coupled quantum dots due to electron-phonon interactions," *Phys. Rev. B*, vol. 72, no. 7, Aug. 2005, Art. no. 075362, doi: 10.1103/PhysRevB.72.075362.

[93] W. M. Witzel and S. Das Sarma, "Quantum theory for electron spin decoherence induced by nuclear spin dynamics in semiconductor quantum computer architectures: Spectral diffusion of localized electron spins in the nuclear solid-state environment," *Phys. Rev. B*, vol. 74, no. 3, Jul. 2006, Art. no. 035322, doi: 10.1103/PhysRevB.74.035322.

[94] J. M. Taylor, J. R. Petta, A. C. Johnson, A. Yacoby, C. M. Marcus, and M. D. Lukin, "Relaxation, dephasing, and quantum control of electron spins in double quantum dots," *Phys. Rev. B*, vol. 76, no. 3, Jul. 2007, Art. no. 035315, doi: 10.1103/PhysRevB.76.035315.

[95] I. P. Gimenez, C.-Y. Hsieh, M. Korkusinski, and P. Hawrylak, "Charged-impurity-induced dephasing of a voltage-controlled coded qubit based on electron spin in a triple quantum dot," *Phys. Rev. B*, vol. 79, no. 20, May 2009, Art. no. 205311, doi: 10.1103/PhysRevB.79.205311.

[96] N. T. T. Nguyen and S. Das Sarma, "Impurity effects on semiconductor quantum bits in coupled quantum dots," *Phys. Rev. B*, vol. 83, no. 23, Jun. 2011, Art. no. 235322, doi: 10.1103/PhysRevB.83.235322.

[97] D. T. Lennon et al., "Efficiently measuring a quantum device using machine learning," *Npj Quantum Inf.*, vol. 5, no. 1, Sep. 2019, Art. no. 79, doi: 10.1038/s41534-019-0193-4.

[98] G. A. Oakes, J. Duan, J. J. L. Morton, A. Lee, C. G. Smith, and M. F. G. Zalba, "Automatic virtual voltage extraction of a 2x2 array of quantum dots with machine learning," May 2021, *arXiv:2012.03685*, doi: 10.48550/arXiv.2012.03685.

[99] O. Krause, A. Chatterjee, F. Kuemmeth, and E. Van Nieuwenburg, "Learning Coulomb diamonds in large quantum dot arrays," *SciPost Phys.*, vol. 13, no. 4, Oct. 2022, Art. no. 84, doi: 10.21468/SciPostPhys.13.4.084.

[100] W. Li et al., "Charge states, triple points, and quadruple points in an InAs nanowire triple quantum dot revealed by an integrated charge sensor," *Adv. Quantum Technol.*, vol. 6, no. 5, 2023, Art. no. 2200158, doi: 10.1002/qute.202200158.

[101] J. Darulova, M. Troyer, and M. C. Cassidy, "Evaluation of synthetic and experimental training data in supervised machine learning applied to charge state detection of quantum dots," May 2020, *arXiv:2005.08131*, doi: 10.48550/arXiv.2005.08131.

[102] J. P. Zwolak, S. S. Kalantre, X. Wu, S. Ragole, and J. M. Taylor, "QFlow lite dataset: A machine-learning approach to the charge states in quantum dot experiments," *PLos One*, vol. 13, no. 10, Oct. 2018, Art. no. e0205844, doi: 10.1371/journal.pone.0205844.

[103] J. Ziegler et al., "Toward robust autotuning of noisy quantum dot devices," *Phys. Rev. Appl.*, vol. 17, no. 2, Feb. 2022, Art. no. 024069, doi: 10.1103/PhysRevApplied.17.024069.

[104] J. R. Johansson, P. D. Nation, and F. Nori, "QuTiP: An open-source Python framework for the dynamics of open quantum systems," *Comput. Phys. Commun.*, vol. 183, no. 8, pp. 1760–1772, Aug. 2012, doi: 10.1016/j.cpc.2012.02.021.

[105] J. R. Johansson, P. D. Nation, and F. Nori, "QuTiP 2: A python framework for the dynamics of open quantum systems," *Comput. Phys. Commun.*, vol. 184, no. 4, pp. 1234–1240, Apr. 2013, doi: 10.1016/j.cpc.2012.11.019.

[106] S. Smidstrup et al., "QuantumATK: An integrated platform of electronic and atomic-scale modelling tools," *J. Phys.: Condens. Matter*, vol. 32, no. 1, Oct. 2019, Art. no. 015901, doi: 10.1088/1361-648X/ab4007.

[107] C. W. Groth, M. Wimmer, A. R. Akhmerov, and X. Waintal, "Kwant: A software package for quantum transport," *New J. Phys.*, vol. 16, no. 6, Jun. 2014, Art. no. 063065, doi: 10.1088/1367-2630/16/6/063065.

[108] S. Birner et al., "Nextnano: General purpose 3-D simulations," *IEEE Trans. Electron Devices*, vol. 54, no. 9, pp. 2137–2142, Sep. 2007, doi: 10.1109/TED.2007.902871.

[109] X. Gao et al., "Quantum computer aided design simulation and optimization of semiconductor quantum dots," *J. Appl. Phys.*, vol. 114, no. 16, Oct. 2013, Art. no. 164302, doi: 10.1063/1.4825209.

[110] E. Nielsen, X. Gao, I. Kalashnikova, R. P. Muller, A. G. Salinger, and R. W. Young, "QCAD simulation and optimization of semiconductor double quantum dots," 2013. [Online]. Available: https://www.osti.gov/biblio/1204068

[111] G. Kiršanskas, J. N. Pedersen, O. Karlström, M. Leijnse, and A. Wacker, "QmeQ 1.0: An open-source Python package for calculations of transport through quantum dot devices," *Comput. Phys. Commun.*, vol. 221, pp. 317–342, Dec. 2017, doi: 10.1016/j.cpc.2017.07.024.

[112] T. Ikegami, K. Fukuda, J. Hattori, H. Asai, and H. Ota, "A TCAD device simulator for exotic materials and its application to a negative-capacitance FET," *J. Comput. Electron.*, vol. 18, no. 2, pp. 534–542, Jun. 2019, doi: 10.1007/s10825-019-01313-7.

[113] H. Asai et al., "Development of integrated device simulator for quantum bit design: Self-consistent calculation for quantum transport and qubit operation," in *Proc. 5th IEEE Electron. Devices Technol. Manuf. Conf.*, Apr. 2021, pp. 1–3, doi: 10.1109/EDTM50988.2021.9420978.

[114] F. Beaudoin et al., "Robust technology computer-aided design of gated quantum dots at cryogenic temperature," *Appl. Phys. Lett.*, vol. 120, no. 26, Jun. 2022, Art. no. 264001, doi: 10.1063/5.0097202.

[115] C. Wasshuber, H. Kosina, and S. Selberherr, "SIMON-A simulator for single-electron tunnel devices and circuits," *IEEE Trans. Comput.-Aided Des. Integr. Circuits Syst.*, vol. 16, no. 9, pp. 937–944, Sep. 1997, doi: 10.1109/43.658562.

[116] P. Eendebak, *QTT Documentation*. Delft, The Netherlands: QuTech, 2023. [Online]. Available: https://qtt.readthedocs.io/en/latest/

[117] B. Khromets, "Heterostructure development and quantum control for semiconductor qubits," M.S. thesis, Dept. Physics Astron., Univ. Waterloo, Waterloo, ON, Canada, 2022. [Online]. Available: https://uwspace.uwaterloo.ca/items/5e74fae1-92c6-46ce-a8da-dd18d2c13360

[118] S. Fleitmann, "Characterization of distortions in charge stability diagrams and their simulation in modeled data," Forschungszentrum Jülich GmbH Zentralbibliothek, Jülich, Germany, Tech. Rep. 4444, 2023, doi: 10.34734/FZJ-2024-00621.

[119] F. Hader et al., "On noise-sensitive automatic tuning of gate-defined sensor dots," *IEEE Trans. Quantum Eng.*, vol. 4, 2023, Art. no. 5500218, doi: 10.1109/TQE.2023.3255743.

[120] T. Botzem et al., "Tuning methods for semiconductor spin qubits," *Phys. Rev. Appl.*, vol. 10, no. 5, Nov. 2018, Art. no. 054026, doi: 10.1103/PhysRevApplied.10.054026.

[121] D. Maradan et al., "GaAs quantum dot thermometry using direct transport and charge sensing," *J. Low Temp. Phys.*, vol. 175, no. 5, pp. 784–798, Jun. 2014, doi: 10.1007/s10909-014-1169-6.

[122] S. Yuan et al., "The characterization of electronic noise in the charge transport through single-molecule junctions," *Small Methods*, vol. 5, no. 3, Mar. 2021, Art. no. 2001064, doi: 10.1002/smtd.202001064.

[123] J. Timmer and M. Koenig, "On generating power law noise," *Astron. Astrophys.*, vol. 300, Aug. 1995, Art. no. 707. [Online]. Available: https://articles.adsabs.harvard.edu//full/1995A%26A...300..707T/0000707.000.html

[124] F. Patzelt, "colorednoise.py," 2017. [Online]. Available: https://github.com/felixpatzelt/colorednoise

[125] X. Chen et al., "Modeling random telegraph noise as a randomness source and its application in true random number generation," *IEEE Trans. Comput.-Aided Des. Integr. Circuits Syst.*, vol. 35, no. 9, pp. 1435–1448, Sep. 2016, doi: 10.1109/TCAD.2015.2511074.

[126] J. B. Johnson, "Thermal agitation of electricity in conductors," *Phys. Rev.*, vol. 32, pp. 97–109, 1928, doi: 10.1103/PhysRev.32.97.

[127] W. Schottky, "Über spontane stromschwankungen in verschiedenen Elektrizitätsleitern," *Ann. Phys.*, vol. 362, pp. 541–567, Jan. 1918, doi: 10.1002/andp.19183622304.

[128] F. Hader, "Simulation of charge stability diagrams for automated tuning solutions," Dec. 2023. [Online]. Available: https://github.com/f-hader/SimCATS

[129] C. Volk et al., "Loading a quantum-dot based "qubYT" register," *Npj Quantum Inf.*, vol. 5, no. 1, 2019, Art. no. 29, doi: 10.5281/zenodo.2620418.

[130] P. Welch, "The use of fast Fourier transform for the estimation of power spectra: A method based on time averaging over short, modified periodograms," *IEEE Trans. Audio Electroacoust.*, vol. AU-15, no. 2, pp. 70–73, Jun. 1967, doi: 10.1109/TAU.1967.1161901.

[131] P. Virtanen et al., "SciPy 1.0: Fundamental algorithms for scientific computing in Python," *Nature Methods*, vol. 17, pp. 261–272, 2020, doi: 10.1038/s41592-019-0686-2.

[132] T. Salimans, I. Goodfellow, W. Zaremba, V. Cheung, A. Radford, and X. Chen, "Improved techniques for training GANs," in *Proc. 30th Int. Conf. Neural Inf. Process. Syst.*, 2016, pp. 2234–2242, doi: 10.5555/3157096.3157346.

[133] M. Heusel, H. Ramsauer, T. Unterthiner, B. Nessler, and S. Hochreiter, "GANs trained by a two time-scale update rule converge to a local Nash equilibrium," in *Proc. 31st Int. Conf. Neural Inf. Process. Syst.*, 2017, pp. 6629–6640, doi: 10.5555/3295222.3295408.

[134] A. M. Alaa, B. van Breugel, E. Saveliev, and M. van der Schaar, "How faithful is your synthetic data? Sample-level metrics for evaluating and auditing generative models," 2021, *arXiv:2102.08921*, doi: 10.48550/arXiv.2102.08921.

[135] L. Ruff, "Pytorch implementation of deep SVDD," 2018. [Online]. Available: https://github.com/lukasruff/Deep-SVDD-PyTorch
[136] L. Ruff et al., "Deep one-class classification," in *Proc. 35th Int. Conf. Mach. Learn.*, 2018, vol. 80, pp. 4393–4402. [Online]. Available: https://proceedings.mlr.press/v80/ruff18a.html
[137] A. Buslaev, A. Parinov, E. Khvedchenya, V. I. Iglovikov, and A. A. Kalinin, "Albumentations: Fast and flexible image augmentations," 2018, *arXiv:1809.06839*, doi: 10.48550/arXiv.1809.06839.
[138] L. Deng, "The MNIST database of handwritten digit images for machine learning research [best of the web]," *IEEE Signal Process. Mag.*, vol. 29, no. 6, pp. 141–142, Nov. 2012, doi: 10.1109/MSP.2012.2211477.

Fabian Hader received the B.Sc. degree in scientific programming and the M.Sc. degree in energy economics and informatics from the FH Aachen—University of Applied Sciences, Jülich, Germany, in 2019 and 2021, respectively. He is currently working toward the Ph.D. degree in engineering with University Duisburg-Essen, Duisburg, Germany.

From 2019 to 2021, he was a Software Engineer with the Central Institute of Engineering, Electronics, and Analytics—Electronic Systems, Forschungszentrum Jülich GmbH, Jülich. His research interests include automatic tuning of quantum dots.

Sarah Fleitmann received the B.Sc. degree in scientific programming and the M.Sc. degree in applied mathematics and informatics from the FH Aachen—University of Applied Sciences, Campus Jülich, Jülich, Germany, in 2020 and 2022, respectively.

Since 2017, she has been a Software Engineer with the Central Institute of Engineering, Electronics and Analytics—Electronic Systems, Forschungszentrum Jülich GmbH, Jülich. Her research interests include the automatic tuning of quantum dots for their operation as qubits.

Jan Vogelbruch received the Dipl.Ing. and Dr.-Ing. degrees in electrical engineering from RWTH Aachen University, Aachen, Germany, in 1994 and 2003, respectively.

In 1995, he joined Parsytec Computer GmbH, Aachen, Germany, as a Technical Project Manager for European cooperations. His focus was on high-performance computing and image processing solutions, and he was the Technical Leader for the company's part in several European-Commission-funded projects. Since late 1998, he has been with the Central Institute of Engineering, Electronics, and Analytics—Electronic Systems, Forschungszentrum Jülich GmbH, Jülich, Germany. His research interests include parallel computing, signal and 3-D image processing, fast reconstruction methods for high-resolution computer tomography, automated defect detection, as well as automatic tuning of semiconductor quantum dots.

Lotte Geck received the B.Sc. and M.Sc. degrees in electrical engineering, information technology and computer engineering from RWTH Aachen University, Aachen, Germany, in 2013 and 2015, respectively, and the Dr.-Ing. degree from the Faculty of Electrical Engineering and Information Technology, RWTH Aachen University, in 2021.

In 2016, she joined the Central Institute of Engineering, Electronics and Analytics—Electronic Systems, Forschungszentrum Jülich GmbH, Jülich, Germany. Since 2022, she has been a Junior Professor with Forschungszentrum Jülich and RWTH Aachen University. Her research interests include scalable electronic system solutions for quantum computing.

Stefan van Waasen received the Diploma and Doctoral degrees in electrical engineering from Gerhard-Mercator University, Duisburg, Germany, in 1994 and 1999, respectively.

The topic of his doctoral thesis was optical receivers up to 60 Gb/s based on traveling-wave amplifiers. In 1998, he joined Siemens Semiconductors/Infineon Technologies AG, Düsseldorf, Germany. His responsibility was BiCMOS and CMOS RF system development for highly integrated cordless systems such as Digital Enhanced Cordless Telecommunications and Bluetooth. In 2001, he changed into the IC development of front-end systems for high-data-rate optical communication systems. From 2004 to 2006, he was with the Stockholm Design Center responsible for the short-range analog, mixed-signal, and RF development for system-on-chip (SoC) CMOS solutions. From 2006 to 2010, he was responsible for the wireless RF system engineering in the area of SoC CMOS products at the headquarters in Munich, Germany, and later with the Design Center Duisburg, Duisburg. Since 2010, he has been the Director of the Central Institute of Engineering, Electronics, and Analytics—Electronic Systems, Forschungszentrum Jülich GmbH, Jülich, Germany. In 2014, he became a Professor for Measurement and Sensor Systems with the Communication Systems Chair, University of Duisburg-Essen, Duisburg. His research interests include complex measurement and detector systems, particularly on electronic systems for quantum computing.